



Prediction of synthesis cross sections of new moscovium isotopes in fusion-evaporation reactions

Peng-Hui Chen^{1,2} · Hao Wu¹ · Zu-Xing Yang³ · Xiang-Hua Zeng^{1,4} · Zhao-Qing Feng⁵

Received: 18 October 2022 / Revised: 24 November 2022 / Accepted: 25 November 2022 / Published online: 13 January 2023

© The Author(s), under exclusive licence to China Science Publishing & Media Ltd. (Science Press), Shanghai Institute of Applied Physics, the Chinese Academy of Sciences, Chinese Nuclear Society 2023

Abstract

In the framework of the dinuclear system model, the synthesis mechanism of the superheavy nuclides with atomic numbers $Z = 112, 114, 115$ in the reactions of projectiles $^{40,48}\text{Ca}$ bombarding on targets ^{238}U , ^{242}Pu , and ^{243}Am within a wide interval of incident energy has been investigated systematically. Based on the available experimental excitation functions, the dependence of calculated synthesis cross-sections on collision orientations has been studied thoroughly. The total kinetic energy (TKE) of these collisions with fixed collision orientation shows orientation dependence, which can be used to predict the tendency of kinetic energy diffusion. The TKE is dependent on incident energies, as discussed in this paper. We applied the method based on the Coulomb barrier distribution function in our calculations. This allowed us to approximately consider all the collision orientations from tip-tip to side-side. The calculations of excitation functions of $^{48}\text{Ca} + ^{238}\text{U}$, $^{48}\text{Ca} + ^{242}\text{Pu}$, and $^{48}\text{Ca} + ^{243}\text{Am}$ are in good agreement with the available experimental data. The isospin effect of projectiles on production cross-sections of moscovium isotopes and the influence of the entrance channel effect on the synthesis cross-sections of superheavy nuclei are also discussed in this paper. The synthesis cross-section of new moscovium isotopes $^{278-286}\text{Mc}$ was predicted to be as large as hundreds of pb in the fusion-evaporation reactions of $^{35,37}\text{Cl} + ^{248}\text{Cf}$, $^{38,40}\text{Ar} + ^{247}\text{Bk}$, $^{39,41}\text{K} + ^{247}\text{Cm}$, $^{40,42,44,46}\text{Ca} + ^{243}\text{Am}$, $^{45}\text{Sc} + ^{244}\text{Pu}$, and $^{46,48,50}\text{Ti} + ^{237}\text{Np}$, $^{51}\text{V} + ^{238}\text{U}$ at some typical excitation energies.

Keywords Dinuclear system model · Superheavy nuclei · Complete fusion reactions · Production cross-section

This work was supported by National Natural Science Foundation of China (Nos. 12105241, 12175072), Natural Science Foundation of Jiangsu Province (No. BK20210788), Jiangsu Provincial Double-Innovation Doctoral Program (No. JSSCBS20211013), University Science Research Project of Jiangsu Province (No. 21KJB140026), Lv Yang Jin Feng (No. YZLYJFJH2021YXBS130), and Key Laboratory of High Precision Nuclear Spectroscopy, Institute of Modern Physics, Chinese Academy of Sciences (No. IMPKFKT2021001).

✉ Peng-Hui Chen
chenpenghui@yzu.edu.cn

Zhao-Qing Feng
fengzhq@scut.edu.cn

¹ School of Physical Science and Technology, Yangzhou University, Yangzhou 225009, China

² Institute of Modern Physics, Chinese Academy of Sciences, Lanzhou 730000, China

³ RIKEN Nishina Center, Wako, Saitama 351-0198, Japan

⁴ College of Electrical, Power and Energy Engineering, Yangzhou University, Yangzhou 225009, China

⁵ School of Physics and Optoelectronics, South China University of Technology, Guangzhou 510641, China

1 Introduction

Since the “island of stability” of superheavy nuclei was predicted by the shell model in the 1960s [1], the synthesis of superheavy nuclei has been an exciting frontier field in the laboratories that could provide a unique tool to explore the properties of nuclei and nuclear structure under extremely strong Coulomb force. However, owing to the extremely low production cross-sections, the synthesis of superheavy nuclei in current experiments is time-consuming and costly. Therefore, it is particularly necessary to make reliable theoretical calculations that provide a reasonable reference for experiments. In recent years, synthesizing superheavy elements through low-energy heavy ion collisions near the Coulomb barrier has attracted extensive attention from theorists and experimentalists.

On the experimental side, in the past half century, fifteen superheavy elements characterized by values of Z in the range 104–118 have been synthesized and identified in laboratories all over the world [2]. Generally, superheavy

synthesis methods are classified by the excitation energy of compound nuclei as cold fusion and hot fusion, resulting in compound nuclei surviving by emitting 1–2 neutrons and 3–5 neutrons, respectively, against fission. Elements Rf, Db, Sg, Fl, Mc, Lv, Ts, and Og were synthesized first in hot-fusion reactions. $^{257,258,259}\text{Rf}$ ($Z = 104$) was discovered simultaneously in Dubna [3] and Berkeley [4] in the reactions of $^{249}\text{Cf}(^{12,13}\text{C}, 3\text{-}4\text{n})^{257,258,259}\text{Rf}$ at incident energy $E_{\text{lab}} = 10.4$ MeV/nucleon. $^{260,261}\text{Db}$ ($Z = 105$) was discovered simultaneously in Dubna [5] and Berkeley [6] in the reactions of $^{249}\text{Cf}(^{15}\text{N}, 4\text{n})^{260}\text{Ds}$ at $E_{\text{lab}} = 85$ MeV and $^{243}\text{Am}(^{22}\text{Ne}, 4\text{n})^{261}\text{Ds}$ at $E_{\text{lab}} = 114$ MeV. ^{263}Sg ($Z = 106$) was discovered at Berkeley [7] in the reactions of $^{249}\text{Cf}(^{18}\text{O}, 4\text{n})^{263}\text{Sg}$ at $E_{\text{lab}} = 95$ MeV. $^{286\text{-}289}\text{Fl}$ was essentially discovered at Dubna [8] in the reactions of $^{244}\text{Pu}(^{48}\text{Ca}, 3\text{-}6\text{n})^{286\text{-}289}\text{Fl}$ at $E_{\text{lab}} = 352.6$ MeV. ^{288}Mc ($Z = 115$) was essentially discovered at Dubna [9] in the reactions of $^{243}\text{Am}(^{48}\text{Ca}, 3\text{n})^{288}\text{Mc}$ at $E_{\text{lab}} = 248, 253$ MeV. $^{286\text{-}289}\text{Lv}$ ($Z = 116$) was discovered at Dubna [10] in the reactions of $^{245}\text{Cm}(^{48}\text{Ca}, x\text{n})^{293\text{-}x}\text{Fl}$ at $E_{\text{lab}} = 243$ MeV. $^{293\text{-}294}\text{Ts}$ ($Z = 117$) was essentially discovered at Dubna [11] in the reactions of $^{249}\text{Bk}(^{48}\text{Ca}, 3\text{-}4\text{n})^{293\text{-}294}\text{Fl}$ at $E_{\text{lab}} = 247, 252$ MeV. ^{294}Og ($Z = 118$) was essentially discovered at Dubna [12] in the reactions of $^{249}\text{Cf}(^{48}\text{Ca}, 3\text{n})^{294}\text{Og}$ at $E_{\text{lab}} = 251$ MeV. Elements Sg, Bh, Hs, Mt, Ds, Rg, Cn, and Nh were synthesized first in cold-fusion reactions. ^{259}Sg ($Z = 106$) was discovered at Dubna [13] in the reactions of $^{207}\text{Pb}(^{54}\text{Cr}, 2\text{n})^{259}\text{Sg}$ at $E_{\text{lab}} = 262$ MeV. ^{262}Bh ($Z = 107$) was essentially discovered at Gesellschaft Für Schwerionenforschung (GSI) [14] in the reactions of $^{209}\text{Bi}(^{54}\text{Cr}, 1\text{n})^{262}\text{Bh}$ at $E_{\text{lab}} = 4.85$ MeV/u. $^{263\text{-}265}\text{Hs}$ ($Z = 108$) was synthesized at GSI [15] in the reactions of $^{208}\text{Pb}(^{58}\text{Fe}, 2\text{n})^{265}\text{Hs}$ at $E_{\text{lab}} = 5.02$ MeV/u. ^{266}Mt ($Z = 109$) was synthesized at GSI [16] in the reactions of $^{209}\text{Bi}(^{58}\text{Fe}, 1\text{n})^{266}\text{Mt}$ at $E_{\text{lab}} = 5.15$ MeV/u. ^{269}Ds ($Z = 110$) was synthesized at GSI [17] in the reactions of $^{208}\text{Pb}(^{62}\text{Ni}, 1\text{n})^{269}\text{Ds}$ at $E_{\text{lab}} = 311$ MeV. ^{272}Rg ($Z = 111$) was synthesized at GSI [18] in the reactions of $^{209}\text{Bi}(^{64}\text{Ni}, 1\text{n})^{272}\text{Rg}$ at $E_{\text{lab}} = 318, 320$ MeV. ^{277}Cn ($Z = 112$) was synthesized at GSI [19] in the reactions of $^{208}\text{Pb}(^{70}\text{Zn}, 1\text{n})^{277}\text{Cn}$ at $E_{\text{lab}} = 344$ MeV. ^{278}Nh ($Z = 113$) was synthesized at RIKEN [20] in the reactions of $^{209}\text{Bi}(^{70}\text{Zn}, 1\text{n})^{278}\text{Nh}$ at $E_{\text{lab}} = 352.6$ MeV. Synthesis information of the most neutron-rich and proton-rich superheavy nuclei with atomic numbers $Z = 104 - 118$, including elements, isotopes, reactions, channels, laboratories, and year, is provided in Table 1. Chinese superheavy nuclei group synthesized the superheavy isotopes of $^{258,259}\text{Db}$ [21], $^{264,265,266}\text{Bh}$ [22], and ^{271}Ds [23] at the Institute of Modern Physics (IMP) (Lanzhou, China).

The mechanism of fusion-evaporation (F.E.) cannot easily reach the next new period in the periodic table of elements because of the limited available combinations of projectile-target. With the development of suitable separation and detection techniques, the multinucleon transfer

(MNT) mechanism might be the most promising method to synthesize unknown superheavy elements. This mechanism has been applied to produce massive heavy and superheavy isotopes [34]. Laboratories all over the world such as IMP [35], GSI [36, 37], Dubna [38, 39], RIKEN [40–42], and Lawrence Berkeley National Laboratory (LBNL) [43, 43] are focused on synthesizing new superheavy elements and their isotopes. From the chart of nuclei, in the superheavy region, there are substantial isotopes of superheavy elements that are still unknown. One of the objectives of the present study was to predict the production cross-sections of moscovium isotopes in F.E. reactions based on different combinations of projectile-target.

On the theoretical side, to describe the production mechanism of superheavy nuclei, some theoretical models were built, for example, the time-dependent Hartree-Fock model [44–46], the improved quantum molecular dynamics model [47–49], a dynamical approach based on Langevin equations [50, 51], and the dinuclear system (DNS) model [52–56]. The calculations resulting from these theoretical models are in good agreement with the available experimental data, which have their own features. In this study, the DNS model has been applied. This model has some advantages such as better consideration of the shell effect, dynamical deformation, fission, quasi-fission, deep-inelastic and odd-even effects, and high calculation efficiency. In previous studies [52, 53, 56–62], the DNS model accurately reproduced the available experimental results and predicted the synthesis production cross-sections of superheavy elements and exotic heavy nuclei in the mechanisms of F.E. and MNT reactions.

In this study, we investigated the dependence of the evaporation residue cross-sections on collision orientations and the influence of entrance channel effect on the evaporation residue cross-sections. We propose a Gaussian-like barrier distribution function for treating the problem of collision orientation dependence. The article is organized as follows. Section 2 briefly describes the DNS model. Calculated results and discussions are presented in Sect. 3. Section 4 concludes the paper with a summary.

2 Model description

Initially, the DNS concept was proposed to describe the deep-inelastic reaction mechanism, which is a molecular-like configuration of two colliding partners, keeping their own individuality in the collision process. The DNS model has been widely used to describe F.E. and multinucleon transfer reactions. The complete fusion evaporation reaction can be described in terms of three processes. First, the colliding partners overcome the Coulomb barrier to form the composite system. Second, the kinetic energy and angular momentum dissipate into the composite system to enable the nucleon transfer between the

Table 1 Synthesis information of the most neutron-rich and proton-rich superheavy isotopes with atomic numbers $Z=104-118$: production reactions, evaporation channel, laboratory, year, and reference

Element	Isotopes	Reactions	Channel	Lab	Year	Ref.
Rf(104)	^{253}Rf	$^{50}\text{Ti} + ^{204}\text{Pb}$	1n	GSI	1997	[24]
(13)	^{267}Rf	$^{48}\text{Ca} + ^{242}\text{Pu}$	α	Dubna	2004	[25]
Db(105)	^{256}Db	$^{50}\text{Ti} + ^{209}\text{Bi}$	3n	GSI	2001	[26]
(11)	^{270}Db	$^{48}\text{Ca} + ^{249}\text{Bk}$	$3n\alpha$	Berkeley	2010	[11]
Sg(106)	^{258}Sg	$^{51}\text{V} + ^{209}\text{Bi}$	2n	GSI	1997	[24]
(12)	^{271}Sg	$^{48}\text{Ca} + ^{238}\text{U}$	α	Dubna	2004	[25]
Bh(107)	^{260}Bh	$^{52}\text{Cr} + ^{209}\text{Bi}$	α	Berkeley	2008	[27]
(10)	^{274}Bh	$^{48}\text{Ca} + ^{249}\text{Bk}$	$3n\alpha$	Dubna	2010	[11]
Hs(108)	^{263}Hs	$^{56}\text{Fe} + ^{208}\text{Pb}$	1n	Berkeley	2009	[28]
(12)	^{277}Hs	$^{48}\text{Ca} + ^{244}\text{Pu}$	$3n\alpha$	GSI	2010	[29]
Mt(109)	^{266}Mt	$^{58}\text{Fe} + ^{209}\text{Bi}$	1n	GSI	1982	[30]
(7)	^{278}Mt	$^{48}\text{Ti} + ^{249}\text{Bk}$	$3n\alpha$	Dubna	2010	[11]
Ds(110)	^{267}Ds	$^{59}\text{Co} + ^{209}\text{Bi}$	1n	Berkeley	1995	[31]
(8)	^{281}Ds	$^{48}\text{Ca} + ^{244}\text{Pu}$	$3n\alpha$	Dubna	2004	[10]
Rg(111)	^{272}Rg	$^{64}\text{Ni} + ^{209}\text{Bi}$	1n	GSI	1995	[32]
(7)	^{282}Rg	$^{48}\text{Ca} + ^{249}\text{Bk}$	$3n\alpha$	Dubna	2010	[11]
Cn(112)	^{277}Cn	$^{70}\text{Zn} + ^{208}\text{Pb}$	1n	GSI	1996	[19]
(6)	^{285}Cn	$^{48}\text{Ca} + ^{244}\text{Pu}$	$3n\alpha$	Dubna	2004	[10]
Nh(113)	^{278}Nh	$^{70}\text{Zn} + ^{209}\text{Bi}$	1n	RIKEN	2004	[33]
(6)	^{286}Nh	$^{48}\text{Ca} + ^{249}\text{Bk}$	$3n\alpha$	Dubna	2010	[11]
Fl(114)	^{285}Fl	$^{48}\text{Ca} + ^{242}\text{Pu}$	5n	Berkeley	2010	[8]
(5)	^{289}Fl	$^{48}\text{Ca} + ^{244}\text{Pu}$	3n	Dubna	2004	[10]
Mc(115)	^{287}Mc	$^{48}\text{Ca} + ^{243}\text{Am}$	4n	Dubna	2004	[9]
(4)	^{290}Mc	$^{48}\text{Ca} + ^{249}\text{Bk}$	$3n\alpha$	Dubna	2010	[11]
Lv(116)	^{290}Lv	$^{48}\text{Ca} + ^{245}\text{Cm}$	3n	Dubna	2004	[10]
(4)	^{293}Lv	$^{48}\text{Ca} + ^{245}\text{Cm}$	1n	Dubna	2004	[10]
Ts(117)	^{293}Ts	$^{48}\text{Ca} + ^{249}\text{Bk}$	4n	Dubna	2010	[11]
(2)	^{294}Ts	$^{48}\text{Ca} + ^{249}\text{Bk}$	3n	Dubna	2010	[11]
Og(118)	^{294}Og	$^{48}\text{Ca} + ^{249}\text{Cf}$	3n	Dubna	2006	[12]

touching colliding partners. Finally, all the nucleons are transferred from projectile nuclei to the target nuclei, which could form the compound nuclei with excitation energy and angular momentum. The highly excited compound nuclei will be de-excited by evaporation of the light particles (i.e., neutrons, γ -rays, and light-charged particles) or fission. Based on the DNS model, the evaporation residual cross-sections of superheavy nuclei can be expressed as

$$\sigma_{\text{ER}}(E_{\text{c.m.}}) = \frac{\pi \hbar^2}{2\mu E_{\text{c.m.}}} \sum_{J=0}^{J_{\text{max}}} (2J + 1) T(E_{\text{c.m.}}, J) P_{\text{CN}}(E_{\text{c.m.}}, J) W_{\text{sur}}(E_{\text{c.m.}}, J), \tag{1}$$

where the penetration probability $T(E_{\text{c.m.}}, J)$ is the probability that the collision system overcomes the Coulomb barrier, which is calculated using the empirical coupling channel model [52]. The fusion probability $P_{\text{CN}}(E_{\text{c.m.}}, J)$ is the

probability to form compound nuclei [63, 64]. The survival probability W_{sur} is the probability that the highly excited compound nuclei survive by evaporating light particles against fission. The maximal angular momentum is set as $J_{\text{max}} = 30-50$ because the fission barrier for the superheavy nuclei may vanish at high spin [65].

2.1 Capture probability

The capture cross-sections of the two colliding partners are expressed as

$$\sigma_{\text{cap}}(E_{\text{c.m.}}) = \frac{\pi \hbar^2}{2\mu E_{\text{c.m.}}} \sum_J (2J + 1) T(E_{\text{c.m.}}, J). \tag{2}$$

Here, the penetration probability $T(E_{\text{c.m.}}, J)$ is evaluated by the Hill-Wheeler formula [66] using the barrier distribution function:

$$T(E_{c.m.}, J) = \frac{\int f(B) dB}{1 + \exp\left\{-\frac{2\pi}{\hbar\omega(J)}\left[E_{c.m.} - B - \frac{\hbar^2 J(J+1)}{2\mu R_B^2(J)}\right]\right\}} \quad (3)$$

where $\hbar\omega(J)$ is the width of the parabolic barrier at position $R_B(J)$. The normalization constant is with respect to the relation $\int f(B)dB = 1$. The barrier distribution function is assumed to be in an asymmetric Gaussian form [52, 67]:

$$f(B) = \begin{cases} \frac{1}{N} \exp\left[-\left(\frac{B-B_m}{\Delta_1}\right)^2\right] & B < B_m, \\ \frac{1}{N} \exp\left[-\left(\frac{B-B_m}{\Delta_2}\right)^2\right] & B > B_m, \end{cases} \quad (4)$$

where $\Delta_2 = (B_0 - B_s)/2$, $\Delta_1 = \Delta_2 - 2 \text{ MeV}$, $B_m = (B_0 + B_s)/2$, and B_0 and B_s are the Coulomb barriers of the side-side collision and saddle-point barriers in dynamical deformations [67]. The nucleus-nucleus interaction potential is expressed as

$$V(\{\alpha\}) = V_C(\{\alpha\}) + V_N(\{\alpha\}) + V_{\text{def}} \quad (5)$$

with

$$V_{\text{def}} = \frac{1}{2} C_1 (\beta_1 - \beta_1^0)^2 + \frac{1}{2} C_2 (\beta_2 - \beta_2^0)^2,$$

where 1 and 2 represent the projectile and target, respectively; $R = R_1 + R_2 + s$ and s are the distances between the center and surface of the projectile and target, respectively; R_1 and R_2 are the radii of the projectile and target, respectively; $\beta_{1(2)}^0$ represents the static deformation of the projectile-target; $\beta_{1(2)}$ represents the adjustable quadrupole deformation, which is varied to find the minimal $V(\{\alpha\})$; and $\{\alpha\}$ stands for $\{R, \beta_1, \beta_2, \theta_1, \theta_2\}$. To reduce the number of deformation variables, we assume that the deformation energy of the colliding system is proportional to its mass [67], that is, $C_1 \beta_1^2 / C_2 \beta_2^2 = A_1 / A_2$. Thus, only one deformation parameter, $\beta = \beta_1 + \beta_2$, is required. The stiffness parameters $C_i (i = 1, 2)$ are calculated using the liquid-drop model [68] through the following parameterization formula:

$$C_i = (\lambda - 1) \left[(\lambda - 1) R_i^2 \sigma - \frac{3}{2\pi} \frac{Z^2 e^2}{R_i (2\lambda + 1)} \right], \quad (6)$$

where R_i is the radius of the spheroidal nucleus given by $R_i = 1.18 A_i^{1/3}$ ($i = 1, 2$). In this study, the quadrupole deformation was taken into account ($\lambda = 2$). Note that σ is the coefficient of surface tension that fits $4\pi r^2 \sigma = a_s A_i^{2/3}$, where $a_s = 18.32 \text{ MeV}$ is the surface energy. The nuclear potential is calculated using the double-folding method [63–65]:

$$V_N = C_0 \left\{ \frac{F_{\text{in}} - F_{\text{ex}}}{\rho_0} \left[\int \rho_1^2(r) \rho_2(r - R) dr + \int \rho_1(r) \rho_2^2(r - R) dR \right] + F_{\text{ex}} \int \rho_1(r) \rho_2(r - R) dr \right\}, \quad (7)$$

where

$$F_{\text{in(ex)}} = f_{\text{in(ex)}} + f'_{\text{in(ex)}} \frac{N_1 - Z_1}{A_1} \frac{N_2 - Z_2}{A_2}.$$

Note the dependence on the nuclear density and orientation of the deformed colliding partners. We set the following parameter values in our calculations: $C_0 = 300 \text{ MeV fm}^3$, $f_{\text{in}} = 0.09$, $f_{\text{ex}} = -2.59$, $f'_{\text{in}} = 0.42$, $f'_{\text{ex}} = 0.54$, and $\rho_0 = 0.16 \text{ fm}^{-3}$. The Woods-Saxon density distribution is expressed as

$$\rho_1(r) = \frac{\rho_0}{1 + \exp[(r - \mathfrak{R}_1(\theta_1))/a_1]} \quad (8)$$

and

$$\rho_2(r - R) = \frac{\rho_0}{1 + \exp[|(r - R) - \mathfrak{R}_2(\theta_2)|/a_2]}, \quad (9)$$

where $\mathfrak{R}_i(\theta_i) (i = 1, 2)$ denotes the surface radii of the nuclei given by $\mathfrak{R}_i(\theta_i) = \mathfrak{R} [1 + \beta_i Y_{20}(\theta_i)]$, where R_i is the spheroidal nuclei radius and a_i is the surface diffuseness coefficient, which was set as 0.55 fm in our calculations. The Coulomb potential was derived by Wong’s formula as follows [69]:

$$V_C(\{\alpha\}) = \frac{Z_1 Z_2 e^2}{r} + \left(\frac{9}{20\pi}\right)^{1/2} \left(\frac{Z_1 Z_2 e^2}{r^3}\right) \sum_{i=1}^2 R_i^2 \beta_i P_2(\cos \theta_i) + \left(\frac{3}{7\pi}\right) \left(\frac{Z_1 Z_2 e^2}{r^3}\right) \sum_{i=1}^2 R_i^2 (\beta_i P_2 \cos \theta_i)^2, \quad (10)$$

where θ_i , β_i , R_i , and $P_2(\cos \theta_i)$ are the angle between the symmetry axis of the deformed projectile-target and collision axis, quadrupole deformation, radius of the projectile-target, and Legendre polynomial, respectively. Wong’s formula is in good agreement with the double-folding method.

2.2 Fusion probability

The composite system is formed after the capture process in which the dissipation of kinetic energy and angular momentum takes place to activate the transfer of nucleons in the touching configuration of the projectile target that results in mass probability diffusion. The mass probability of the formed fragments was evaluated by solving a set of master equations. The term of

mass probability $P(Z_1, N_1, E_1, t)$ contains the proton number, neutron numbers of Z_1 and N_1 , and internal excitation energy of E_1 for a given fragment A_1 . The master equation is [57, 64, 70]

$$\begin{aligned} & \frac{dP(Z_1, N_1, E_1, t)}{dt} \\ &= \sum_{Z'_1} W_{Z_1, N_1; Z'_1, N'_1}(t) [d_{Z_1, N_1} P(Z'_1, N_1, E'_1, t) \\ & \quad - d_{Z'_1, N'_1} P(Z_1, N_1, E_1, t)] \\ & \quad + \sum_{N'_1} W_{Z_1, N_1; Z_1, N'_1}(t) [d_{Z_1, N_1} P(Z_1, N'_1, E'_1, t) \\ & \quad - d_{Z_1, N'_1} P(Z_1, N_1, E_1, t)] \\ & \quad - [\Lambda_{A_1, E_1, t}^{qf}(\Theta) + \Lambda_{A_1, E_1, t}^{fis}(\Theta)] P(Z_1, N_1, E_1, t), \end{aligned} \tag{11}$$

where $W_{Z_1, N_1; Z'_1, N'_1}$ ($W_{Z_1, N'_1; Z_1, N_1}$) denotes the mean transition probability from the channel (Z_1, N_1, E_1) to (Z'_1, N_1, E'_1) [or (Z_1, N_1, E_1) to (Z_1, N'_1, E'_1)]; d_{Z_1, N_1} denotes the microscopic dimension corresponding to the macroscopic state (Z_1, N_1, E_1) . The sum contains all possible numbers of protons and neutrons for fragment (Z'_1, N'_1) . However, only one nucleon transfer at one time is assumed in the model with relations $Z'_1 = Z_1 \pm 1$, and $N'_1 = N_1 \pm 1$. The excitation energy E_1 is the local excitation energy ϵ_1^* for fragment (Z'_1, N'_1) , which is derived by the dissipation of the relative motion along with the potential energy surface (PES) of the DNS [71]. The time of the dissipation process is evaluated by the parameterization classical deflection function [72]. The motion of nucleons in the interaction potential is governed by the single-particle Hamiltonian:

$$H(t) = H_0(t) + V(t), \tag{12}$$

where the total single-particle energy and interaction potential are

$$H_0(t) = \sum_K \sum_{v_K} \epsilon_{v_K}(t) \alpha_{v_K}^+(t) \alpha_{v_K}(t), \tag{13}$$

$$\begin{aligned} V(t) &= \sum_{K, K'} \sum_{\alpha_K, \beta_{K'}} u_{\alpha_K, \beta_{K'}} \alpha_{\alpha_K}^+(t) \alpha_{\beta_{K'}}(t) \\ &= \sum_{K, K'} V_{K, K'}(t), \end{aligned} \tag{14}$$

where ϵ_{v_K} and $u_{\alpha_K, \beta_{K'}}$ represent the single-particle energies and interaction matrix elements, respectively, in which the single-particle state is defined as center of colliding nuclei assumed to be orthogonal in the overlapping region. The annihilation and creation operators are time-dependent. The single-particle matrix elements are parameterized as

$$\begin{aligned} u_{\alpha_K, \beta_{K'}} &= U_{K, K'}(t) \\ &\times \left\{ \exp \left[-\frac{1}{2} \left(\frac{\epsilon_{\alpha_K}(t) - \epsilon_{\beta_{K'}}(t)}{\Delta_{K, K'}(t)} \right)^2 \right] - \delta_{\alpha_K, \beta_{K'}} \right\}, \end{aligned} \tag{15}$$

where $U_{K, K'}(t)$ and $\delta_{\alpha_K, \beta_{K'}}(t)$ are described in Ref. [73]. The proton transition probability is microscopically derived from

$$\begin{aligned} W_{Z_1, N_1; Z'_1, N'_1} &= \frac{\tau_{\text{mem}}(Z_1, N_1, E_1; Z'_1, N_1, E'_1)}{d_{Z_1, N_1} d_{Z'_1, N'_1} \hbar^2} \\ &\times \sum_{ii'} |\langle Z'_1, N_1, E'_1, i' | V | Z_1, N_1, E_1, i \rangle|^2. \end{aligned} \tag{16}$$

The neutron transition probability has a similar formula. The memory time and interaction elements V are described in Ref. [63].

The evolution of the DNS along distance R leads to quasi-fission. The decay probability of quasi-fission is calculated based on the one-dimensional Kramers equation as [73, 74]

$$\begin{aligned} \Lambda_{A_1, E_1, t}^{qf}(\Theta) &= \frac{\omega}{2\pi\omega^{B_{qf}}} \left[\sqrt{\left(\frac{\Gamma}{2\hbar} \right)^2 + (\omega^{B_{qf}})^2} - \frac{\Gamma}{2\hbar} \right] \\ &\times \exp \left[-\frac{B_{qf}(A_1)}{\Theta(A_1, E_1, t)} \right], \end{aligned} \tag{17}$$

where $B_{qf}(A_1)$ is the quasi-fission barrier; ω and $\omega^{B_{qf}}$ are the frequencies of the harmonic oscillator approximation at the bottom and top of the interaction potential pocket, which are constants expressed as $\hbar\omega^{B_{qf}} = 2.0$ MeV and $\hbar\omega = 3.0$ MeV in this study; $\Gamma = 2.8$ MeV is the quantity characterizing the average double width of the single-particle state. The local temperature is expressed using the Fermi gas model, i.e., $\Theta = (\epsilon^*/(A/12))^{1/2}$. In the nuclear collision process, heavy fragments might lead to fission; the fission probability is calculated by the Kramers formula:

$$\begin{aligned} \Lambda_{A_1, E_1, t}^{fis}(\Theta) &= \frac{\omega_{g.s.}}{2\pi\omega_f} \left[\sqrt{\left(\frac{\Gamma_0}{2\hbar} \right)^2 + (\omega_f)^2} - \frac{\Gamma_0}{2\hbar} \right] \\ &\times \exp \left[-\frac{B_f(A_1)}{\Theta(A_1, E_1, t)} \right], \end{aligned} \tag{18}$$

where $\omega_{g.s.}$ and ω_f are the frequencies of the oscillators approximating the fission-path potential at the ground state and top of the fission barrier for fragment A_1 , respectively, which were set as $\hbar\omega_{g.s.} = \hbar\omega_f = 1.0$ MeV and $\Gamma_0 = 2$ MeV. The fission barrier is calculated by the macroscopic part plus the shell correction energy. In the relaxation process of the relative motion, the DNS is excited by the dissipation of the relative kinetic energy and angular momentum. The excited composite system opens a valence space $\Delta\epsilon_K$ in

fragment K ($K = 1, 2$) that has a symmetrical distribution around the Fermi surface. The nucleons in the valence space are actively enabled to be excited and transferred. The average of these quantities is performed in the valence space:

$$\Delta\epsilon_K = \sqrt{\frac{4\epsilon_K^*}{g_K}}, \quad \epsilon_K^* = \epsilon^* \frac{A_K}{A}, \quad g_K = A_K/12, \quad (19)$$

where ϵ^* is the local excitation energy of the DNS, which provides the excitation energy for the mean transition probability. There are $N_K = g_K \Delta\epsilon_K$ valence states and $m_K = N_{K/2}$ valence nucleons in the valence space $\Delta\epsilon_K$, leading to dimensions

$$d(m_1, m_2) = \binom{N_1}{m_1} \binom{N_2}{m_2}. \quad (20)$$

The local excitation energy is expressed as

$$\epsilon^* = E_x - (U_{\text{dr}}(A_1, A_2) - U_{\text{dr}}(A_P, A_T)), \quad (21)$$

where $U_{\text{dr}}(A_1, A_2)$ and $U_{\text{dr}}(A_P, A_T)$ are the driving potentials of fragments A_1, A_2 and A_P, A_T , respectively. The detailed calculations of the driving potentials are given by Eq. 22. The excitation energy E_x of the composite system is converted from the relative kinetic energy dissipation [64]. The PES of the DNS is expressed as

$$U_{\text{dr}}(A_1, A_2; J, \theta_1, \theta_2) = B_1(N_1, Z_1, \beta_1) + B_2(N_2, Z_2, \beta_2) - B_{\text{CN}}(N, Z, \beta) + U_C(Z_1, Z_2, \beta_1, \beta_2, R, \theta_1, \theta_2) + U_N(Z_1, Z_2, \beta_1, \beta_2, R, \theta_1, \theta_2), \quad (22)$$

where B_i ($i = 1, 2$) and B_{CN} are the negative binding energies of fragment A_i and compound nucleus $A = A_1 + A_2$, respectively, where the shell and pairing corrections are reasonably included; β_i represents the quadrupole deformations of binary fragments; θ_i denotes collision orientations; and U_C and U_N are derived from Eqs. 10 and 7, respectively.

By solving a set of master equations, the probability of all possible formed fragments is obtained. The hindrance in the fusion process is named inner fusion barrier, B_{fus} , which is defined by the difference from the injection position to the B.G. point. In the DNS model, these fragments overcome the inner barrier that is considered to lead to fusion. Therefore, the fusion probability is evaluated by adding all the fragments that could penetrate the inner fusion barrier:

$$P_{\text{CN}}(E_{\text{c.m.}}, J, B) = \sum_{Z=1}^{Z_{\text{BG}}} \sum_{N=1}^{N_{\text{BG}}} P(N_1, Z_1, E_1(J), \tau_{\text{int}}(J)). \quad (23)$$

Here, the interaction time $\tau_{\text{int}}(E_{\text{c.m.}}, J, B)$ is obtained from the deflection function method [71]. We calculated the fusion probability as

$$P_{\text{CN}}(E_{\text{c.m.}}, J) = \int f(B) P_{\text{CN}}(E_{\text{c.m.}}, J, B) dB. \quad (24)$$

The Coulomb barrier distribution function $f(B)$ is given by Eq. 4. Therefore, the fusion cross-section is expressed as

$$\sigma_{\text{fus}}(E_{\text{c.m.}}) = \sigma_{\text{cap}}(E_{\text{c.m.}}) P_{\text{CN}}(E_{\text{c.m.}}, J). \quad (25)$$

2.3 Survival probability

The compound nuclei are formed by all the transfers of nucleons from projectile nuclei to target nuclei that have a few excitation energies. The excited compound nuclei are extremely unstable and can be de-excited by evaporating γ -rays, neutrons, protons, α , etc., against fission. The survival probability of the channel x -th neutron, y -th proton, and z -th α is expressed as [57, 70, 75]

$$W_{\text{sur}}(E_{\text{CN}}^*, x, y, z, J) = P(E_{\text{CN}}^*, x, y, z, J) \times \prod_{i=1}^x \frac{\Gamma_n(E_i^*, J)}{\Gamma_{\text{tot}}(E_i^*, J)} \prod_{j=1}^y \frac{\Gamma_p(E_j^*, J)}{\Gamma_{\text{tot}}(E_j^*, J)} \prod_{k=1}^z \frac{\Gamma_\alpha(E_k^*, J)}{\Gamma_{\text{tot}}(E_k^*, J)}, \quad (26)$$

where E_{CN}^* and J denote the excitation energy and spin of the excited nucleus, respectively. The total width Γ_{tot} is the sum of the partial widths of particle evaporation, γ -rays, and fission. The excitation energy E_s^* before evaporating the s -th particles is evaluated by

$$E_{s+1}^* = E_s^* - B_i^n - B_j^p - B_k^\alpha - 2T_s, \quad (27)$$

with initial condition $E_i^* = E_{\text{CN}}^*$ and $s = i + j + k$; B_i^n , B_j^p , and B_k^α denote the separation energies of the i -th neutron, j -th proton, and k -th alpha, respectively. The nuclear temperature T_i is defined by $E_i^* = \alpha T_i^2 - T_i$ with level density α . The decay width of γ -rays and the particle decay were evaluated with a method similar to that reported in Ref. [75]. We set $E^* - B_v - \delta - \delta_n$ to the term ρ .

The widths of particles decay are evaluated using the Weisskopf evaporation theory as

$$\Gamma_v(E^*, J) = (2s_v + 1) \frac{m_v}{\pi^2 \hbar^2 \rho(E^*, J)} \times \int_0^{\rho - \frac{1}{a}} \epsilon \rho(\rho + \delta - E_{\text{rot}} - \epsilon, J) \sigma_{\text{inv}}(\epsilon) d\epsilon. \quad (28)$$

Here, s_v , m_v , and B_v are the spin, mass, and binding energy of the particle, respectively. The pairing correction energy δ was set to be $12/\sqrt{A}$, 0, and $-12/\sqrt{A}$ for even-even, even-odd, and odd-odd nuclei, respectively. The inverse cross-section is expressed as $\sigma_{\text{inv}} = \pi R_v^2 T(v)$.

The penetration probability was set to 1 for neutrons and $T(\nu) = (1 + \exp(\pi(V_C(\nu) - \epsilon)/\hbar\omega))^{-1}$ for charged particles with $\hbar\omega = 5$ and 8 MeV for proton and α , respectively. The Coulomb barrier of the emitting charge particles and daughter nuclei is expressed as

$$V_C = \frac{(Z_{CN} - i)Z_i e^2}{r_i (A_{CN-i}^{1/3} + A_i^{1/3})}. \tag{29}$$

In this study, we set proton emitting $r_p = 1.7$ fm and α emitting $\alpha = 1.75$ fm; for further information, please refer to [76]. The fission width was calculated using the Bohr-Wheeler formula, as in Ref. [63, 64]. We set $E^* - B_f - E_{rot} - \delta - \delta_f$ to the term κ .

$$\Gamma_f(E^*, J) = \frac{1}{2\pi\rho_f(E^*, J)} \int_0^{\kappa - \frac{1}{a_f}} \frac{\rho_f(\kappa - \epsilon + \delta, J) d\epsilon}{1 + \exp[-2\pi(\kappa - \epsilon + \delta + \delta_f)/\hbar\omega]} \tag{30}$$

For heavy fragments, the fission width is usually set as $\hbar\omega = 2.2$ MeV [77], and δ_f denotes the pairing correction for the fission barrier. The fission barrier is divided into microscopic and macroscopic parts:

$$B_f(E^*, J) = B_f^{LD} + B_f^M(E^* = 0, J) \exp(-E^*/E_D), \tag{31}$$

where the macroscopic part is derived from the liquid-drop model:

$$B_f^{LD} = \begin{cases} 0.38(0.75 - x)E_{S0}, & (1/3 < x < 2/3) \\ 0.83(1 - x)^3 E_{S0}, & (2/3 < x < 1) \end{cases} \tag{32}$$

with

$$x = \frac{E_{C0}}{2E_{S0}}. \tag{33}$$

Here, E_{C0} and E_{S0} are the Coulomb energy and surface energy of the spherical nuclear, respectively, which could be taken from the Myers-Swiatecki formula:

$$E_{S0} = 17.944 \left[1 - 1.7826 \left(\frac{N - Z}{A} \right)^2 \right] A^{2/3} \text{ MeV} \tag{34}$$

and

$$E_{C0} = 0.7053 \frac{Z^2}{A^{1/3}} \text{ MeV}. \tag{35}$$

The microcosmic shell correction energy was taken from [78]. The shell-damping energy was

$$E_D = \frac{5.48A^{1/3}}{1 + 1.3A^{-1/3}} \text{ MeV} \tag{36}$$

or

$$E_D = 0.4A^{4/3}/a \text{ MeV} \tag{37}$$

where a is the energy level density parameter. The fission level density was set as $a_f = 1.1a$. The moments of inertia of fission compound nuclei at ground state (gs) and saddle point (sd) configurations are expressed as

$$\zeta_{gs(sd)} = k \times \frac{2}{5} m r^2 \left(1 + \beta_2^{gs(sd)}/3 \right). \tag{38}$$

Here, $k = 0.4$ is the correction factor of the rigid body and β_2 is the quadrupole deformation taken from Ref. [78]; $\beta_2^{sd} = \beta_2^{gs} + 0.2$ was the quadrupole deformation at the saddle point calculated by the relativistic mean field theory. Based on the Fermi gas model, the energy level density could be expressed as [78]

$$\rho(E^*, J) = K_{coll} \times \frac{2J + 1}{24\sqrt{2}\sigma^3 a^{1/4} (E^* - \delta)^{5/4}} \times \exp \left[2\sqrt{a(E^* - \delta)} - \frac{(J + 1/2)^2}{2\sigma^2} \right], \tag{39}$$

where $\sigma^2 = 6\bar{m}^2 \sqrt{a(E^* - \delta)}/\pi^2$ and $\bar{m} \approx 0.24A^{2/3}$; K_{coll} is the collective enhancement factor, which contains the rotational and vibration effects. The level density parameter is set as $a = A/12$, $a_f = 1.1a$ for the fission-level density parameter.

The realization probability of evaporation channels is an important component in the survival probability equation. The realization probability of one particle evaporation is expressed as

$$P(E_{CN}^*, J) = \exp \left[-\frac{(E_{CN}^* - B_s - E_{rot} - 2T)^2}{2\sigma^2} \right], \tag{40}$$

where σ is the half-height width of the excitation function of the residual nucleon in the F.E. reactions, which was set as 2.5 MeV in our calculations, and E_{rot} is the rotation energy. For the multiple neutron evaporation channels ($x > 1$), the realization probability can be derived using the Jackson formula:

$$P(E_{CN}^*, s, J) = I(\Delta_s, 2s - 3) - I(\Delta_{s+1}, 2s - 1), \tag{41}$$

where I and Δ are given by

$$I(z, m) = \frac{1}{m!} \int_0^z u^m e^{-u} du, \tag{42}$$

$$\Delta_s = \frac{E_{CN}^* - \sum_{i=1}^s B_i^v}{T_i}, \tag{43}$$

where B_i^v is the separation energy of the evaporation of the i -th particle and $s=x+y+z$. The spectrum of realization probabilities determines the distribution shape of survival probability in the evaporation channels.

3 Results and discussion

In the framework of the DNS model involving all the collision orientations, we calculated the excitation functions of 2n-, 3n-, 4n-, and 5n-evaporation channels for the collisions of $^{48}\text{Ca}+^{243}\text{Am}$, $^{48}\text{Ca}+^{242}\text{Pu}$, and $^{48}\text{Ca}+^{238}\text{U}$, marked by solid olive, dash red, dash-dot blue, and orange short-dash lines, respectively, in Fig. 1. In panel (a), the olive-filled up-triangle, red-filled square, and blue-filled circle represent experimental results of 2n-, 3n-, and 4n-evaporation channels for $^{48}\text{Ca}+^{243}\text{Am}$ taken from Ref. [9, 83, 84]. According to Ref. [9], the experiments concerning $^{48}\text{Ca}+^{243}\text{Am}$ at incident energies $E_{\text{lab}} = 248, 253$ MeV were carried out at FLNR, JINR. At $E_{\text{lab}} = 248$ MeV, three similar decay chains consisting of five consecutive α decays were identified. At $E_{\text{lab}} = 253$ MeV, the decay properties of these synthesized nuclei are consistent with consecutive α decays originating from the parent isotopes of the new element, Mc, i.e., ^{287}Mc and ^{288}Mc , produced in the 3n- and 4n-evaporation channels with cross-sections of approximately 3 pb and 1 pb, respectively. According to Ref. [83], the cross-section for the 3n-evaporation channel reaches its maximum, $\sigma_{3n} = 8.5^{+6.4}_{-3.7}$ pb, at $E^* = 34.0 - 38.3$ MeV and decreases with further increase in the excitation energy of the compound nucleus ^{291}Mc . At excitation energy, $E^* = 44.8 \pm 2.3$ MeV, not a single event indicating the formation of ^{288}Mc was detected. The upper cross section limit can thus be set at level $\sigma_{3n} \leq 1$ pb. At excitation energy in the range of $E^* = 31.1 - 36.4$ MeV, the cross

sections for the formation of ERs in the 3n- and 2n-evaporation channels were approximately $3.5^{+2.7}_{-1.5}$ pb and $2.5^{+2.7}_{-1.5}$ pb, respectively. At energies $E^* \leq 36$ MeV, which could be expected for the 2n-evaporation product, ^{289}Mc was not detected. The upper cross section limit can be set at level $\sigma_{2n} \leq 3$ pb. According to Ref. [84], the cross sections for the formation of ERs in the 3n- and 2n-evaporation channels are approximately $3.2^{+0.8}_{-1.2}$ pb and $0.3^{+0.7}_{-0.2}$ pb at energies $E^* = 33$ MeV, respectively. In Fig. 1 (b), the olive up-triangle, red square, blue circle, and orange down-triangle represent the experimental results of 2n-, 3n-, 4n-, and 5n-evaporation channels for $^{48}\text{Ca}+^{242}\text{Pu}$, respectively, where filled, half-filled, and open symbols represent three experiments for $^{48}\text{Ca}+^{242}\text{Pu}$ [8, 79, 80, 86]. According to Ref. [79], a maximum cross section of $10.4^{+3.5}_{-2.1}$ pb was measured for $^{242}\text{Pu}(^{48}\text{Ca}, 3n)^{287}\text{Fl}$ reaction. According to Ref. [8], at excitation energy $E^* = 50$ MeV, $^{242}\text{Pu}(^{48}\text{Ca}, 5n)^{285}\text{Fl}$ cross section was $0.6^{+0.9}_{-0.5}$ pb. The no-observation of a 3n-evaporation product led to an upper limit for $^{242}\text{Pu}(^{48}\text{Ca}, 3n)^{287}\text{Fl}$ reaction of 1.1 pb. The 3n and 4n cross section values measured at $E^* = 41$ MeV were $3.1^{+4.9}_{-2.6}$ pb. In Fig. 1 (c), the red square and blue circle stand for the experimental results of 3n- and 4n-evaporation channels for $^{48}\text{Ca}+^{238}\text{U}$, respectively, where filled, half-filled, and open symbols represent three experiments for $^{48}\text{Ca}+^{238}\text{U}$ [79–82]. According to Ref. [80], the maximum cross section values of the xn-evaporation channels for the reaction $^{238}\text{U}(^{48}\text{Ca}, xn)^{286-x}\text{Cn}$ were measured to be $\sigma_{3n} = 2.5^{+1.8}_{-1.1}$ pb and $\sigma_{4n} = 0.6^{+1.6}_{-0.5}$ pb. At the excitation energies of the compound nucleus $E^* = 34.5$ MeV, two decay events from ^{283}Cn were observed, resulting in a cross section of $2.0^{+2.7}_{-1.3}$ pb [82]. The cross section deduced from all four events was $0.72^{+0.58}_{-0.35}$ pb, measured at an excitation energy of 34.6 MeV of the compound nucleus ^{286}Cn [81]. From the above three panels, we can conclude that our calculations are in

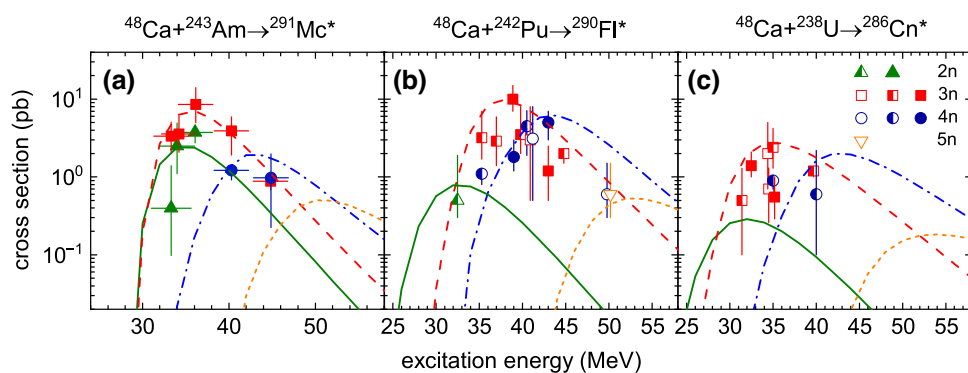


Fig. 1 (Color Online) The calculated excitation functions of 2n-, 3n-, 4n-, and 5n-evaporation channels for the reactions of $^{48}\text{Ca}+^{243}\text{Am}$, $^{48}\text{Ca}+^{242}\text{Pu}$, and $^{48}\text{Ca}+^{238}\text{U}$ are marked by solid olive, dash red, dash-dot blue, and orange short-dash lines, respectively. The experimental measurement results of excitation functions for 2n-, 3n-, 4n-, and

5n-evaporation channels are represented by an up-triangle, square, circle, and down-triangle. Vertical error bars correspond to total uncertainties. Symbols with arrows show upper cross-section limits. Data marked by open, half-closed, and filled symbols are taken from [8, 9, 79–85], respectively

good agreement with the available experimental excitation functions of the reactions $^{48}\text{Ca}+^{243}\text{Am}$, $^{48}\text{Ca}+^{242}\text{Pu}$, and $^{48}\text{Ca}+^{238}\text{U}$.

To investigate the dependence of the production cross section of superheavy nuclei in F.E. reactions on collision orientation, we exported four configurations of the collision orientations from our calculations for the reaction of $^{48}\text{Ca}+^{243}\text{Am}$ as $(0^\circ, 0^\circ)$, $(30^\circ, 30^\circ)$, $(60^\circ, 60^\circ)$ and $(90^\circ, 90^\circ)$, marked by the solid black, red dash, olive dash-dot, and blue short-dash lines, respectively, in Fig. 2. The projectile nuclei ^{48}Ca and target nuclei ^{243}Am have theoretical quadrupole deformation values $\beta_p = 0$. and $\beta_T = 0.224$, respectively. In Fig. 2, panel (a) shows the distributions of interaction potential energy with respect to the distance between the surfaces of projectile nuclei and target nuclei. The interaction potential V_{CN} consists of Coulomb potential V_C and nucleus-nucleus potential V_N , which are calculated by Wong's formula [69] and the double-folding method [87], respectively. The interaction potential energies were increased with the large collision orientations because of the large effective interaction face. Panel (b) displays the distributions of radial kinetic energy with respect to the interaction time. The kinetic energy decreased exponentially with increasing reaction time at the prescribed impact parameter, i.e., $L = 20 \hbar$. These evolutions of kinetic energy reached equilibrium at approximately $2 \times 10^{-21}\text{s}$. These equilibrium kinetic energies were 225 MeV, 228 MeV, 235 MeV, and 239 MeV, corresponding to collision orientations $(0^\circ, 0^\circ)$, $(30^\circ, 30^\circ)$, $(60^\circ, 60^\circ)$, and $(90^\circ, 90^\circ)$, respectively. The kinetic energy dissipated into the internal excitation of the composite system, which correspondingly increased exponentially with the reaction time for the same relaxation time, as illustrated in panel (c). According to Fig. 2, we can conclude that the

interaction potential and evolution of kinetic energy and internal excitation energy were highly dependent on the orientations. These were the basic reasons causing the dependence of the final synthesis cross sections of superheavy nuclei on collision orientations.

The PES and driving potential (DP) of the reaction $^{48}\text{Ca}+^{243}\text{Am}$ were calculated by Eq. 22 for the collision orientations of sphere-sphere, $(0^\circ, 0^\circ)$, $(30^\circ, 30^\circ)$, $(60^\circ, 60^\circ)$ and $(90^\circ, 90^\circ)$, as illustrated in Fig. 3. The PES and DP are listed in the upper and lower panels, respectively. Panels (a) and (f) show the PES and DP of the no-deformation of projectile-target nuclei. The minimum trajectories and injection points are attached to the PESs, which are represented by solid black lines and filled black stars. The structure effect is clearly shown in the PESs and DPs by the comparison of no-deformation collision with quadrupole deformation collision. The inner fusion barrier was set as the difference between the injection points and Businaro-Gallone (B.G.) points, which were 8 MeV, 11.5 MeV, 10.5 MeV, 7.1 MeV, and 6 MeV corresponding to collision orientations of no-deformation, $(0^\circ, 0^\circ)$, $(30^\circ, 30^\circ)$, $(60^\circ, 60^\circ)$, and $(90^\circ, 90^\circ)$, respectively. It was found that the inner fusion barrier was highly dependent on the collision orientations, which could reveal the fusion probability directly. The inner fusion barriers were decreased with the increased collision orientation, reaching its minimum at the waist-waist collision. Sketches of collision orientations are shown at the top of Fig. 3. The potential energy of the symmetry field in the PES increased with increasing collision orientations because the corresponding Coulomb force increased as well.

In the collision process, when overcoming the Coulomb barrier, the kinetic energies of the colliding partners rapidly dissipate into the composite system. The probability

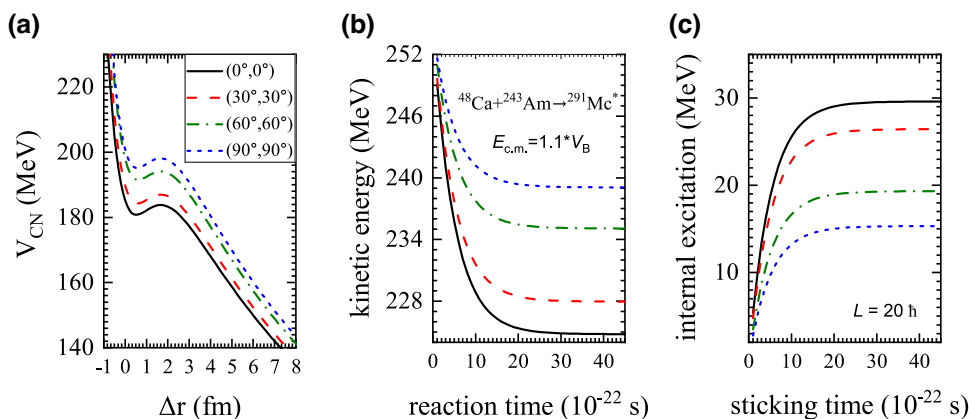


Fig. 2 (Color Online) Panel **a** shows the interaction potential for the collisions of $^{48}\text{Ca}+^{243}\text{Am}$ as a function of distance with different collision angles. The collision orientations $(0^\circ, 0^\circ)$, $(30^\circ, 30^\circ)$, $(60^\circ, 60^\circ)$, and $(90^\circ, 90^\circ)$ correspond to solid black, red dash, olive dash-dot, and short dash lines, respectively. Panel **b** represents the radial kinetic

energy decreases along with the reaction time at different collision orientations under an angular momentum $L = 20 \hbar$. Panel **c** shows that the internal excitation energy of the composite system varies with the sticking time for the given angular momentum $L = 20 \hbar$

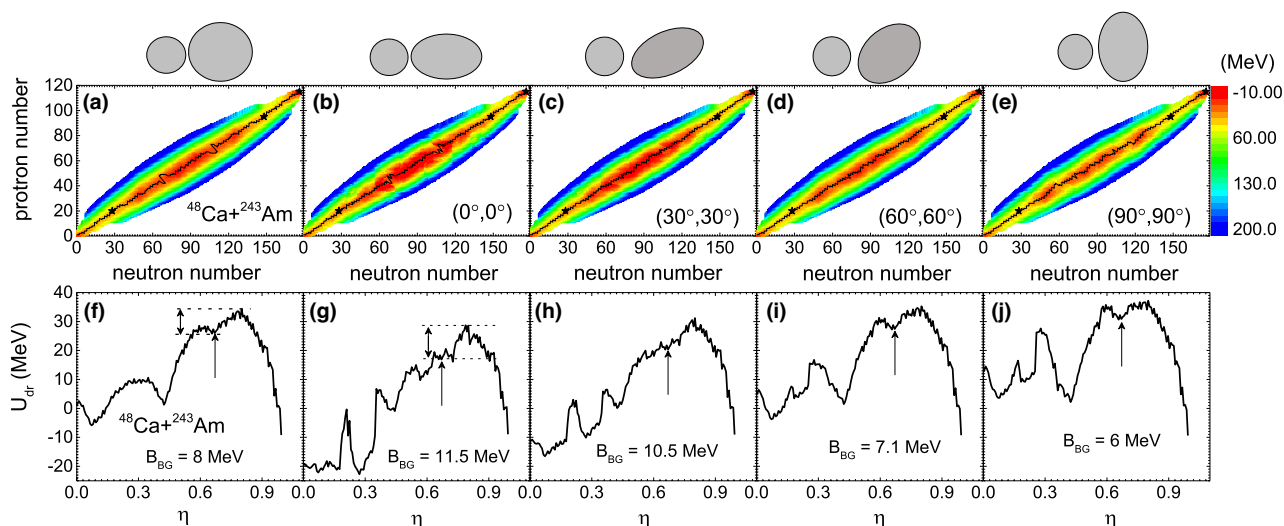


Fig. 3 (Color Online) Panels **a**, **b**, **c**, **d**, and **e** represent the PES of $^{48}\text{Ca}+^{243}\text{Am}$ at collision orientations of sphere-sphere, $(0^\circ, 0^\circ)$, $(30^\circ, 30^\circ)$, $(60^\circ, 60^\circ)$, and $(90^\circ, 90^\circ)$, respectively. Panels **f**, **g**, **h**, **i**, and **j** correspond to their collision orientation-based valley tra-

jectories in PES along with the mass asymmetry η with respect to $\eta = (A_T - A_P)/(A_T + A_P)$. Their inner barrier value is given by B_{BG} . The arrow lines represent injection points

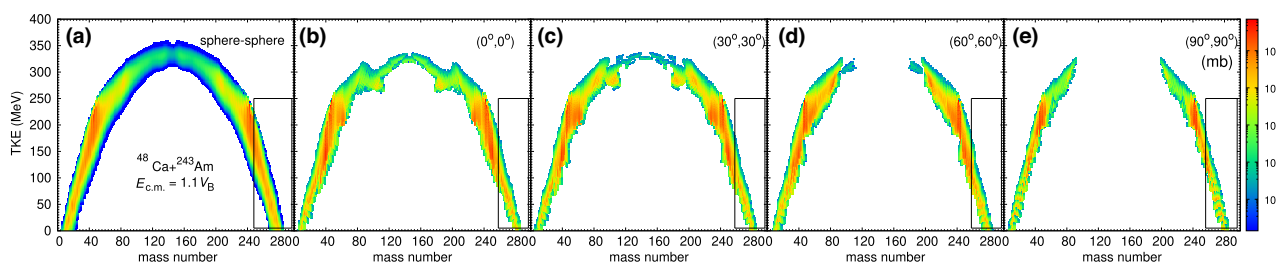


Fig. 4 (Color Online) Panels **a**, **b**, **c**, **d**, and **e** display the calculations of TKE-mass distribution of the primary fragments in the collisions of $^{48}\text{Ca}+^{243}\text{Am}$ at $E_{c.m.} = 1.1 \times V_B$ for their collision orientations of sphere-sphere, $(0^\circ, 0^\circ)$, $(30^\circ, 30^\circ)$, $(60^\circ, 60^\circ)$, and $(90^\circ, 90^\circ)$, respectively

of projectile and target diffusing along the PES was calculated by solving a set of master equations. The TKE of binary fragments was related to the incident energy, ground-state binding energy, and internal excitation energy as $TKE = E_{c.m.} - V_{CN} - Q_{gg} - E^*$. Figure 4 presents the TKE-mass distributions for collision orientations of no-deformation, $(0^\circ, 0^\circ)$, $(30^\circ, 30^\circ)$, $(60^\circ, 60^\circ)$, and $(90^\circ, 90^\circ)$ at incident energy $E_{c.m.} = 1.1 \times V_B$, as shown in panels (a), (b), (c), (d), and (e), respectively. The TKE term could be rewritten as $TKE = E_{c.m.} - U_{dr} - E^*$. The TKE-mass distribution shape is highly dependent on the driving potential. The TKE-mass distribution for no-deformation collision in panel (a) was smoother than others in panels (b), (c), (d), and (e), thereby showing the structure effect in the TKE-mass distribution. The fragments in the black square passing the B.G. points are supposed to lead to fusion. The fusion probability was calculated by summing all the formation probabilities passing B.G. points. Figure 4 reveals that it is difficult to evaluate

the dependence of fusion probability on the collision orientations; the reason is that only one incident energy, $E_{c.m.} = 1.1 \times V_B$, is shown.

Figure 5 shows the TKE-mass distributions at excitation energies $E_{CN}^* = 10$ MeV, 40 MeV, 70 MeV, and 100 MeV for the tip-tip collisions of $^{48}\text{Ca}+^{243}\text{Am}$, as illustrated in panels (a), (b), (c), and (d), respectively. Figure 5 shows that the TKE-mass distribution was broader for increasing incident energy. It is evident that the fusion probability increased with larger excitation energy. However, the compound nuclei with large excitation energy could easily lead to fission. The maximum evaporation residue cross section of the high-excitation compound nuclei was the balance between fusion probability and survival probability.

To approximate the real collision process as much as possible, we propose Gaussian-like barrier distributions to consider all the collision orientations. Equation (4) can be employed for this purpose. The olive solid, red

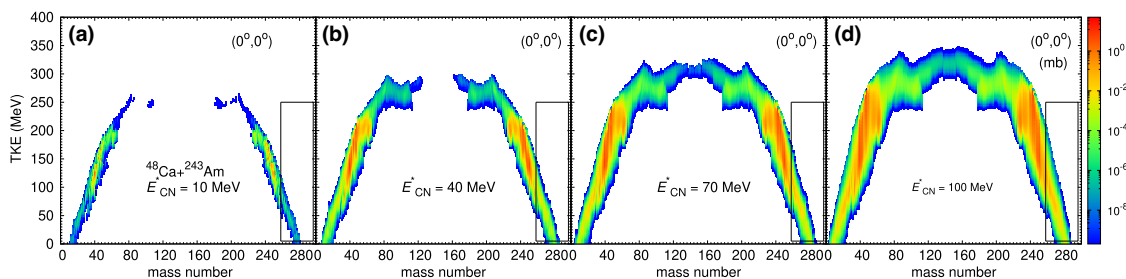


Fig. 5 (Color Online) Panels **a**, **b**, **c**, and **d** show the calculations of TKE-mass distribution of the primary fragments in the head-on collisions of $^{48}\text{Ca}+^{243}\text{Am}$ at incident energies corresponding to excitation

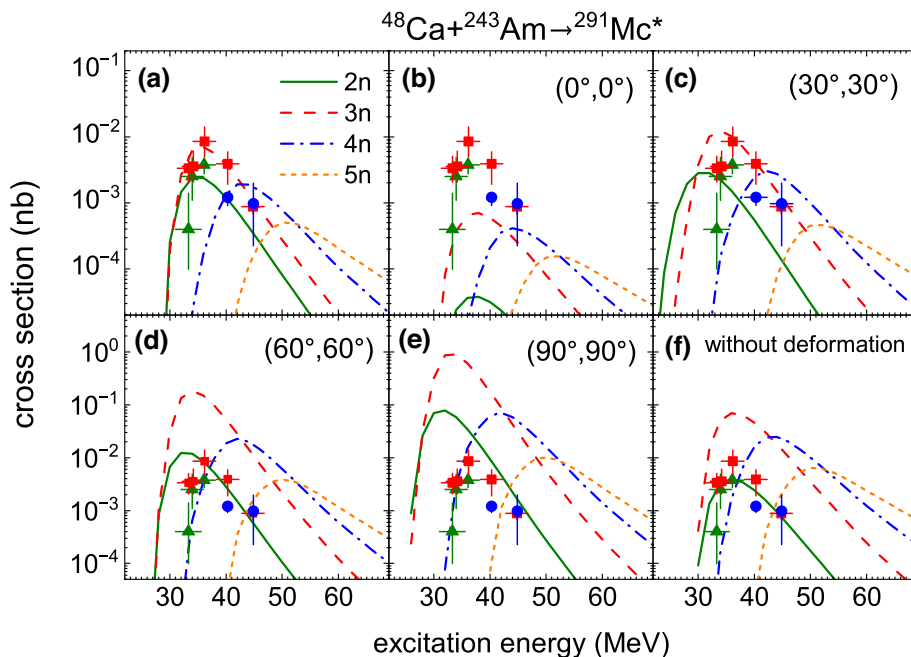
energies of compound nuclei, that is, 10 MeV, 40 MeV, 70 MeV, and 100 MeV, respectively

dash, blue dot-dash, and orange short-dash lines represent the calculated excitation function of the 2n-, 3n-, 4n-, and 5n-evaporation channels. The olive-filled up-triangle, red-filled square, and blue-filled circle represent the experimental excitation function of the 2n-, 3n-, and 4n-evaporation channels, respectively. For the reactions $^{48}\text{Ca}+^{243}\text{Am}$ at excitation energies within the interval $E^* = 20\text{--}100$ MeV, the excitation functions of the 2n-, 3n-, 4n-, and 5n-evaporation channels were calculated by the DNS model involving the barrier distribution, as shown in panel (a); these functions are in good agreement with the experimental data [9, 83]. The calculated excitation functions of $^{48}\text{Ca}+^{243}\text{Am}$ for the collision orientations $(0^\circ, 0^\circ)$, $(30^\circ, 30^\circ)$, $(60^\circ, 60^\circ)$, $(90^\circ, 90^\circ)$, and no-deformation are shown in panels (b), (c), (d), (e), (f), respectively. It was found that $(0^\circ, 0^\circ)$ collisions underestimate the experimental results. Collisions $(30^\circ, 30^\circ)$ agree with the

experimental results relatively well. Collisions $(30^\circ, 30^\circ)$, $(60^\circ, 60^\circ)$, and $(90^\circ, 90^\circ)$ overestimate the experimental data. Figure 6 shows that the DNS model involving barrier distributions could reproduce the experimental results relatively well.

Based on the DNS model involving barrier distribution, to investigate the dependence of evaporation residue cross section on the isospin of the projectile, we systematically calculated the reactions of $^{42}\text{Ca}+^{243}\text{Am}$, $^{44}\text{Ca}+^{243}\text{Am}$, $^{46}\text{Ca}+^{243}\text{Am}$, $^{48}\text{Ca}+^{243}\text{Am}$, $^{44}\text{Ti}+^{237}\text{Np}$, $^{46}\text{Ti}+^{237}\text{Np}$, $^{48}\text{Ti}+^{237}\text{Np}$, and $^{50}\text{Ti}+^{237}\text{Np}$ at excitation energies within the interval $E^* = 1\text{--}80$ MeV. Figure 7 shows that the excitation functions of the evaporation residue cross section are highly dependent on the isospin of the projectile. Regarding the isotopes of Ca-induced reactions, the cross sections of 2n- and 3n-evaporation channels decreased with the projectile of Ca isotopes with large N/Z , which might be caused by fusion

Fig. 6 (Color Online) For the collisions of $^{48}\text{Ca}+^{243}\text{Am}$, the panels show the calculations of excitation functions in 2n-, 3n-, 4n-, and 5n-evaporation channels corresponding to solid olive, red dash, blue dash-dot, and orange short-dash lines, respectively. Panels **b**, **c**, **d**, **e**, and **f** display the excitation functions at orientations $(0^\circ, 0^\circ)$, $(30^\circ, 30^\circ)$, $(60^\circ, 60^\circ)$, $(90^\circ, 90^\circ)$, and sphere to sphere, respectively. Panel (a) shows the total excitation function when considering all the collision orientations using the method of Gaussian distribution. Experimental data are marked by filled up-triangle, square, circle, and down-triangle symbols, as in [9, 83]



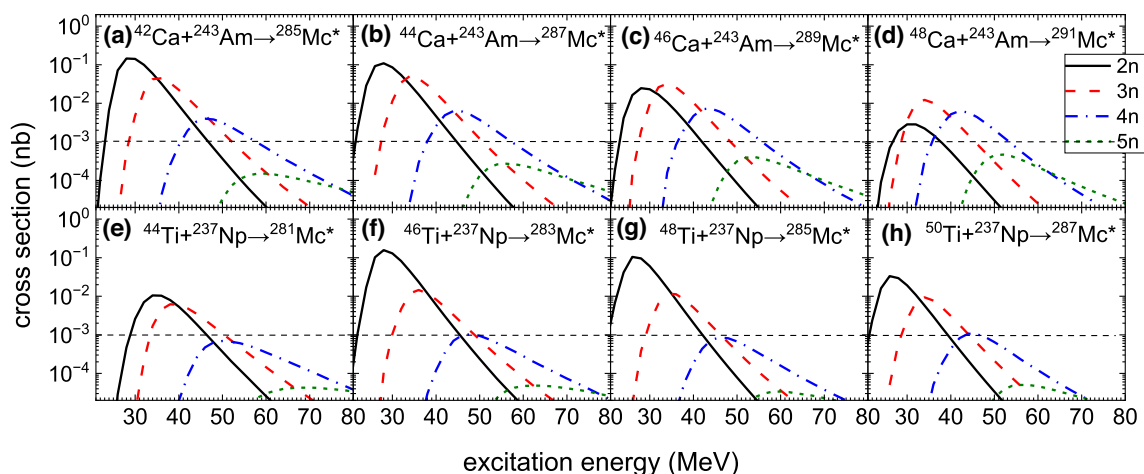


Fig. 7 (Color Online) The calculations of excitation functions for the collisions of $^{42}\text{Ca}+^{243}\text{Am}$, $^{44}\text{Ca}+^{243}\text{Am}$, $^{46}\text{Ca}+^{243}\text{Am}$, $^{48}\text{Ca}+^{243}\text{Am}$, $^{44}\text{Ti}+^{237}\text{Np}$, $^{46}\text{Ti}+^{237}\text{Np}$, $^{48}\text{Ti}+^{237}\text{Np}$, and $^{50}\text{Ti}+^{237}\text{Np}$ are shown in pan-

els **a, b, c, d, e, f, g** and **h** respectively. The 2n-, 3n-, 4n-, and 5n-evaporation channels correspond to black solid, red dash, blue dash-dot, and olive short-dash lines, respectively

probability. The ratio of σ_{3n}/σ_{2n} increased with increasing N/Z , which implies that more-neutron-rich compound nuclei are prone to evaporating more neutrons. The existing moscovium isotopes are $^{287-290}\text{Mc}$. The predictions of maximum cross sections of the new $^{281-286}\text{Mc}$ were 4 pb, 45 pb, 150 pb, 50 pb, 101 pb, and 30 pb, respectively, in calcium-isotope-induced F.E. reactions. The maximum synthesis cross section of new moscovium isotopes was ^{283}Mc as 0.15 nb in the reactions $^{42}\text{Ca}+^{243}\text{Am}$. Concerning Ti-isotope induced reactions, the 2n-evaporation channel was dominant in the evaporation residue cross sections. The maximum synthesis cross section of Mc was ^{281}Mc as 0.2 nb in the reactions $^{46}\text{Ti}+^{237}\text{Np}$. The new moscovium isotopes of $^{278-286}\text{Mc}$ were evaluated as 0.5 pb, 9 pb, 12 pb, 10.5 pb, 150 pb, 11 pb,

100 pb, 10 pb, and 31 pb, respectively, in titanium-isotope-induced F.E. reactions.

To investigate the influence of the entrance effect on the synthesis cross section of superheavy moscovium in the F.E. reactions, we systematically calculated the collisions of $^{35}\text{Cl}+^{248}\text{Cf}$ ($\eta = 0.75$), $^{40}\text{Ar}+^{247}\text{Bk}$ ($\eta = 0.72$), $^{39}\text{K}+^{247}\text{Cm}$ ($\eta = 0.73$), $^{40}\text{Ca}+^{243}\text{Am}$ ($\eta = 0.72$), $^{48}\text{Ca}+^{243}\text{Am}$ ($\eta = 0.67$), $^{45}\text{Sc}+^{244}\text{Pu}$ ($\eta = 0.69$), $^{48}\text{Ti}+^{237}\text{Np}$ ($\eta = 0.66$), and $^{51}\text{V}+^{238}\text{U}$ ($\eta = 0.65$) based on the DNS model, as illustrated in panels (a), (b), (c), (d), (e), (f), (g), and (h), respectively. Figure 8 shows that the reaction systems with large η are prone to producing large production cross-sections because the large mass asymmetry reactions are in turn prone to fusion. In these calculations, the

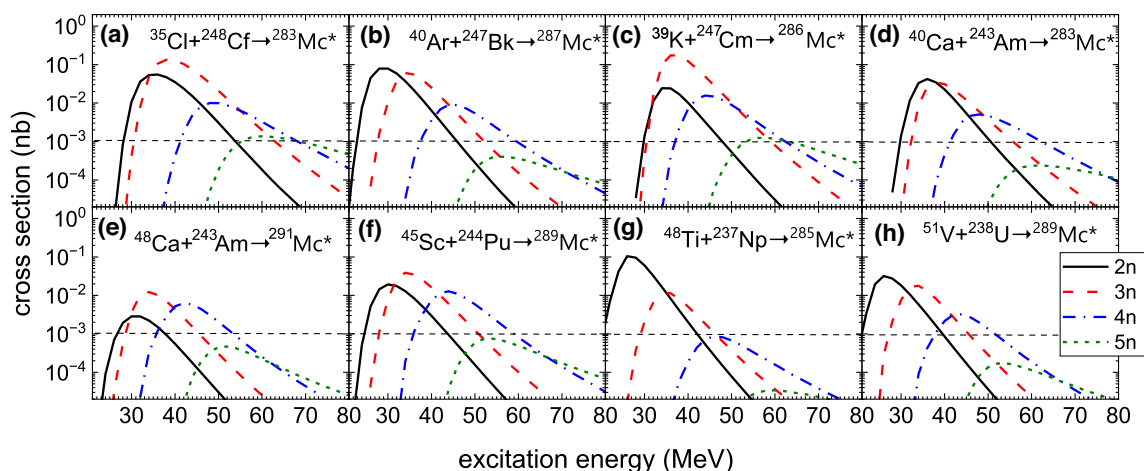


Fig. 8 (Color Online) The calculations of excitation functions in the collisions of $^{35}\text{Cl}+^{248}\text{Cf}$, $^{40}\text{Ar}+^{247}\text{Bk}$, $^{39}\text{K}+^{247}\text{Cm}$, $^{40}\text{Ca}+^{243}\text{Am}$, $^{48}\text{Ca}+^{243}\text{Am}$, $^{45}\text{Sc}+^{244}\text{Pu}$, $^{48}\text{Ti}+^{237}\text{Np}$, and $^{51}\text{V}+^{238}\text{U}$ are shown in pan-

els **a, b, c, d,** and **e, f, g** and **h**, respectively. The 2n-, 3n-, 4n-, and 5n-evaporation channels correspond to black solid, red dash, blue dash-dot, and olive short-dash lines, respectively

new moscovium $^{278-286}\text{Mc}$ was predicted with production cross section values of 1 pb, 10 pb, 130 pb, 50 pb, 15 pb, 100 pb, 30 pb, 200 pb, 40 pb, respectively. The 2n- or 3n-evaporation residue channels were dominant in the evaporation survival process. The ratio σ_{3n}/σ_{2n} illustrates the role of the odd-even effect on the production cross section of superheavy nuclei. The maximum production cross section of moscovium isotopes was predicted as 200 pb in the reaction $^{247}\text{Cm}(^{39}\text{K}, 3n)^{283}\text{Mc}$.

4 Conclusion

As a summary, to simulate the real collision process, we propose a Gaussian-like barrier distribution function used to include all collision orientations. To investigate the dependence of the production cross section of superheavy isotopes on the collision orientations, we systematically calculated the reactions of $^{48}\text{Ca}+^{243}\text{Am}$ at excitation energies within the interval 0-100 MeV for the collision orientations of no-deformation, i.e., $(0^\circ, 0^\circ)$, $(30^\circ, 30^\circ)$, $(60^\circ, 60^\circ)$, and $(90^\circ, 90^\circ)$. In the DNS model, for a given collision orientation, some physical quantities such as interaction potential, radial kinetic energy, internal excitation energy, TKE-mass, PES, DP, and inner fusion barrier were exported to show the influence of collision orientations; the conclusion is that these quantities are highly dependent on the collision orientations. We compared the calculated excitation functions of $^{48}\text{Ca}+^{243}\text{Am}$ at some fixed collision orientations with available experimental results. We found that large collision orientations showed an overestimated value compared to experimental data. The collision orientation nearby $(30^\circ, 30^\circ)$ fit the experimental data very well. The barrier-distribution-based excitation function was in good agreement with the experimental data. To test the barrier distribution function, we calculated the reactions of $^{48}\text{Ca}+^{243}\text{Pu}$ and $^{48}\text{Ca}+^{238}\text{U}$, which reproduced the experimental excitation functions well. Based on the DNS model involving the barrier distribution function, we systematically calculated the reactions of projectiles $^{42-48}\text{Ca}$ bombarding on target ^{243}Am and projectiles $^{42-48}\text{Ca}$ on target ^{237}Np . The influence of the isospin of a projectile on the production cross section was studied. For Ca-induced F.E. reactions, σ_{2n} and σ_{3n} were dominant in the evaporation residue cross sections, which decreased with increasing N/Z in projectiles. The ratio σ_{3n}/σ_{2n} increased with increasing N/Z in projectiles, which might be caused by neutron-rich compound nuclei prone to losing neutrons. For Ti-induced F.E. reactions, the maximum cross section was 150 pb for ^{283}Mc in the reaction $^{237}\text{Np}(^{46}\text{Ti}, 2n)^{283}\text{Mc}$. The reactions of $^{35}\text{Cl}+^{248}\text{Cf}$, $^{40}\text{Ar}+^{247}\text{Bk}$, $^{39}\text{K}+^{247}\text{Cm}$, $^{40}\text{Ca}+^{243}\text{Am}$, $^{48}\text{Ca}+^{243}\text{Am}$, $^{45}\text{Sc}+^{244}\text{Pu}$, $^{48}\text{Ti}+^{237}\text{Np}$, and $^{51}\text{V}+^{238}\text{U}$ were calculated to investigate the entrance

channel effect on production cross sections of superheavy nuclei. Large mass asymmetry systems lead to large production cross section. We also found that the odd-even effect might play a role in the evaporation residue cross section. We predicted the new moscovium isotopes $^{278-286}\text{Mc}$ with maximum cross sections of 0.5 pb, 9 pb, 12 pb, 10.5 pb, 150 pb, 11 pb, 100 pb, 10 pb, and 31 pb in the collisions of $^{35,37}\text{Cl} + ^{248}\text{Cf}$, $^{38,40}\text{Ar} + ^{247}\text{Bk}$, $^{39,41}\text{K} + ^{247}\text{Cm}$, $^{40,42,44,46}\text{Ca} + ^{243}\text{Am}$, $^{45}\text{Sc} + ^{244}\text{Pu}$, and $^{46,48,50}\text{Ti} + ^{237}\text{Np}$, $^{51}\text{V} + ^{238}\text{U}$ at some typical excitation energies.

Author Contributions All authors contributed to the study conception and design. Material preparation, data collection and analysis were performed by Peng-Hui Chen, Hao Wu, and Zu-Xing Yang. The first draft of the manuscript was written by Peng-Hui Chen and all authors commented on previous versions of the manuscript. All authors read and approved the final manuscript.

References

1. Y.T. Oganessian, V.K. Utyonkov, Super-heavy element research. Reports Progr. Phys. **78**, 036301 (2015). <https://doi.org/10.1088/0034-4885/78/3/036301>
2. M. Thoennessen, Discovery of isotopes of elements with $Z \geq 100$. Atomic Data Nucl. Data Tables **99**, 312–344 (2013). <https://doi.org/10.1016/j.adt.2012.03.003>
3. G. Heinlein, K. Bächmann, J. Rudolph, in *Superheavy Elements*, Model experiments with short-lived nuclides for the investigation of the quantitative chemical behaviour of new elements. (Pergamon, 1978), pp. 407–414 <https://doi.org/10.1016/B978-0-08-022946-1.50051-7>
4. A. Ghiorso, M. Nurmi, K. Eskola et al., 261rf; new isotope of element 104. Phys. Lett. B **32**, 95–98 (1970). [https://doi.org/10.1016/0370-2693\(70\)90595-2](https://doi.org/10.1016/0370-2693(70)90595-2)
5. G.N. Flerov, Y.T. Oganessian, Y.V. Lobanov et al., Synthesis of element 105. Sov. At. Energy **29**, 967–975 (1970). <https://doi.org/10.1007/BF01154430>
6. A. Ghiorso, M. Nurmi, K. Eskola et al., New element hahnium, atomic number 105. Phys. Rev. Lett. **24**, 1498–1503 (1970). <https://doi.org/10.1103/PhysRevLett.24.1498>
7. A. Ghiorso, J.M. Nitschke, J.R. Alonso et al., Element 106. Phys. Rev. Lett. **33**, 1490–1493 (1974). <https://doi.org/10.1103/PhysRevLett.33.1490>
8. P.A. Ellison, K.E. Gregorich, J.S. Berryman et al., New super-heavy element isotopes: $^{242}\text{Pu}(^{48}\text{Ca}, 5n)^{285}114$. Phys. Rev. Lett. **105**, 182701 (2010). <https://doi.org/10.1103/PhysRevLett.105.182701>
9. Y.T. Oganessian, V.K. Utyonkov, Y.V. Lobanov et al., Experiments on the synthesis of element 115 in the reaction $^{243}\text{Am}(^{48}\text{Ca}, xn)^{291-x}115$. Phys. Rev. C **69**, 021601 (2004). <https://doi.org/10.1103/PhysRevC.69.021601>
10. Y.T. Oganessian, V.K. Utyonkov, Y.V. Lobanov et al., Measurements of cross sections for the fusion-evaporation reactions $^{244}\text{Pu}(^{48}\text{Ca}, xn)^{292-x}114$ and $^{245}\text{Cm}(^{48}\text{Ca}, xn)^{293-x}116$. Phys. Rev. C **69**, 054607 (2004). <https://doi.org/10.1103/PhysRevC.69.054607>
11. Y.T. Oganessian, F.S. Abdullin, P.D. Bailey et al., Synthesis of a new element with atomic number $Z=117$. Phys. Rev. Lett. **104**, 142502 (2010). <https://doi.org/10.1103/PhysRevLett.104.142502>
12. Y.T. Oganessian, V.K. Utyonkov, Y.V. Lobanov et al., Synthesis of the isotopes of elements 118 and 116 in the ^{249}Cf and $^{245}\text{Cm}+^{48}$

- Ca fusion reactions. *Phys. Rev. C* **74**, 044602 (2006). <https://doi.org/10.1103/PhysRevC.74.044602>
13. Y.T. Oganessian, Y.P. Tretyakov, A.S. Ilinov, et al., Synthesis of neutron-deficient isotopes of fermium, kurchatovium, and element 106. *JETP Lett. (USSR)* **20**, 265 (1975)
 14. G. Münzenberg, S. Hofmann, F.P. Heßberger et al., Identification of element 107 by α correlation chains. *Zeitschrift für Physik A Hadrons and Nuclei* **300**, 107–108 (1981). <https://doi.org/10.1007/BF01412623>
 15. G. Münzenberg, P. Armbruster, H. Folger et al., The identification of element 108. *Zeitschrift für Physik A Atoms and Nuclei* **317**, 235–236 (1984). <https://doi.org/10.1007/BF01421260>
 16. G. Münzenberg, P. Armbruster, F.P. Hessberger et al., Observation of one correlated α -decay in the reaction ^{209}Bi on $^{267}\text{109}$. *Zeitschrift für Physik A Atoms and Nuclei* **309**, 89–90 (1982). <https://doi.org/10.1007/BF01420157>
 17. S. Hofmann, V. Ninov, F. Heßberger et al., Production and decay of $^{269}\text{110}$. *Zeitschrift für Physik A Hadrons and Nuclei* **350**, 277–280 (1995). <https://doi.org/10.1007/BF01291181>
 18. S. Hofmann, V. Ninov, F. Heßberger et al., The new element 111. *Zeitschrift für Physik A Hadrons and Nuclei* **350**, 281–282 (1995). <https://doi.org/10.1007/BF01291182>
 19. S. Hofmann, V. Ninov, F. P. Heßberger et al., The new element 112. *Zeitschrift für Physik A Hadrons and Nuclei* **354**, 229–230 (1996). <https://doi.org/10.1007/BF02769517>
 20. K. Morita, K. Morimoto, D. Kaji, et al., Experiment on the synthesis of element 113 in the reaction $^{209}\text{Bi}(^{70}\text{Zn}, n)^{278}\text{113}$. *Journal of the Physical Society of Japan* **73**, 2593–2596 (2004). <https://doi.org/10.1143/JPSJ.73.2593>
 21. Z. Gan, Z. Qin, H. Fan et al., A new alpha-particle - emitting isotope ^{259}Db . *Eur. Phys. J. A* **10**, 21–25 (2001). <https://doi.org/10.1007/s100500170140>
 22. Q. Zhi, W. Xiao Lie, D. Hua Jie et al., Alpha decay properties of ^{266}Bh . *Nucl. Phys. Rev.* **23**, 404 (2006). <https://doi.org/10.11804/NuclPhysRev.23.04.404>
 23. Z.Y. Zhang, Z.G. Gan, L. Ma et al., Observation of the superheavy nuclide ^{271}Ds . *Chin. Phys. Lett.* **58**, 87 (2012). <https://doi.org/10.1088/0256-307X/29/1/012502>
 24. F.P. Heßberger, S. Hofmann, V. Ninov et al., Spontaneous fission and alpha-decay properties of neutron deficient isotopes $^{257-253}\text{104}$ and $^{258}\text{106}$. *Zeitschrift für Physik A Hadrons and Nuclei* **359**, 415–425 (1997). <https://doi.org/10.1007/s002180050422>
 25. U. Tippawan, S. Pomp, A. Ataç et al., Light-ion production in the interaction of 96 MeV neutrons with silicon. *Phys. Rev. C* **69**, 064609 (2004). <https://doi.org/10.1103/PhysRevC.69.064609>
 26. F.P. Heßberger, S. Hofmann, D. Ackermann et al., Decay properties of neutron-deficient isotopes $^{256,257}\text{Db}$, ^{255}Rf , $^{252,253}\text{Lr}$. *Eur. Phys. J. A - Hadrons Nucl.* **12**, 57–67 (2001). <https://doi.org/10.1007/s100500170039>
 27. S.L. Nelson, K.E. Gregorich, I. Dragojević et al., Lightest isotope of bh produced via the $^{209}\text{Bi}(^{52}\text{Cr}, n)^{260}\text{Bh}$ reaction. *Phys. Rev. Lett.* **100**, 022501 (2008). <https://doi.org/10.1103/PhysRevLett.100.022501>
 28. I. Dragojević, K.E. Gregorich, C.E. Düllmann et al., New isotope ^{263}Hs . *Phys. Rev. C* **79**, 011602 (2009). <https://doi.org/10.1103/PhysRevC.79.011602>
 29. C.E. Düllmann, M. Schädel, A. Yakushev et al., Production and decay of element 114: High cross sections and the new nucleus ^{277}Hs . *Phys. Rev. Lett.* **104**, 252701 (2010). <https://doi.org/10.1103/PhysRevLett.104.252701>
 30. G. Münzenberg, P. Armbruster, F. Heßberger et al., Observation of one correlated α -decay in the reaction ^{58}Fe on ^{209}Bi \rightarrow $^{267}\text{109}$. *Zeitschrift für Physik A Hadrons and Nuclei* **309**, 89–90 (1982)
 31. A. Ghiorso, D. Lee, L.P. Somerville et al., Evidence for the possible synthesis of element 110 produced by the $^{59}\text{Co}+^{209}\text{Bi}$ reaction. *Phys. Rev. C* **51**, R2293–R2297 (1995). <https://doi.org/10.1103/PhysRevC.51.R2293>
 32. J. Corish, G.M. Rosenblatt, Name and symbol of the element with atomic number 111. *Pure Appl. Chem.* **76**, 2101–2103 (2004). <https://doi.org/10.1351/pac200476122101>
 33. K. Morita, K. Morimoto, D. Kaji et al., Experiment on the synthesis of element 113 in the reaction $^{209}\text{Bi}(^{70}\text{Zn}, n)^{278}\text{113}$. *J. Phys. Soc. Japan* **73**, 2593–2596 (2004). <https://doi.org/10.1143/jpsj.73.2593>
 34. V.V. Volkov, Deep inelastic transfer reactions - the new type of reactions between complex nuclei. *Phys. Rep.* **44**, 93–157 (1978). [https://doi.org/10.1016/0370-1573\(78\)90200-4](https://doi.org/10.1016/0370-1573(78)90200-4)
 35. Z. Gan, W. Huang, Z. Zhang et al., Results and perspectives for study of heavy and super-heavy nuclei and elements at IMP/CAS. *Eur. Phys. J. A* **58**, 84 (2022). <https://doi.org/10.1140/epja/s10050-022-00811-w>
 36. S. Heinz, H. Devaraja, Nucleosynthesis in multinucleon transfer reactions. *Eur. Phys. J. A* **58**, 114 (2022). <https://doi.org/10.1140/epja/s10050-022-00771-1>
 37. M. Block, F. Giacoppo, F.P. Heßberger et al., Recent progress in experiments on the heaviest nuclides at SHIP. *Nuovo Cimento Rivista Serie* **45**, 279–323 (2022). <https://doi.org/10.1007/s40766-022-00030-5>
 38. B. Sergey, S. Dmitriev, N. Kazarinov et al., She factory: Cyclotron facility for super heavy elements research. 2020. <https://doi.org/10.18429/JACoW-Cyclotrons2019-THC01>
 39. G. Adamyan, N. Antonenko, A. Diaz-Torres et al., How to extend the chart of nuclides? *Eur. Phys. J. A* **56**, 1–47 (2020). <https://doi.org/10.1140/epja/s10050-020-00046-7>
 40. D. Kaji, K. Morimoto, A. Yoneda et al., Target for the heaviest element production at RIKEN. *Nucl. Instrum. Meth. Phys. Res. Sect. A* **590**, 198–203 (2008). <https://doi.org/10.1016/j.nima.2008.02.090>
 41. H. Haba, A new period in superheavy-element hunting. *Nat. Chem.* **11**, 10–13 (2019). <https://doi.org/10.1038/s41557-018-0191-8>
 42. T. Tanaka, K. Morita, K. Morimoto et al., Study of quasielastic barrier distributions as a step towards the synthesis of superheavy elements with hot fusion reactions. *Phys. Rev. Lett.* **124**, 052502 (2020). <https://doi.org/10.1103/PhysRevLett.124.052502>
 43. J.L. Pore, J.M. Gates, R. Orford et al., Identification of the new isotope ^{244}Md . *Phys. Rev. Lett.* **124**, 252502 (2020). <https://doi.org/10.1103/PhysRevLett.124.252502>
 44. L. Guo, C. Simenel, L. Shi et al., The role of tensor force in heavy-ion fusion dynamics. *Phys. Lett. B* **782**, 401–405 (2018). <https://doi.org/10.1016/j.physletb.2018.05.066>
 45. K. Sekizawa, Tdhf theory and its extensions for the multinucleon transfer reaction: A mini review. *Front. Phys.* **7**, 20 (2019). <https://doi.org/10.3389/fphy.2019.00020>
 46. J. Maruhn, P.G. Reinhard, P. Stevenson et al., The tdhf code sky3d. *Computer Phys. Commun.* **185**, 2195–2216 (2014). <https://doi.org/10.1016/j.cpc.2014.04.008>
 47. N. Wang, Z. Li, X. Wu, Improved quantum molecular dynamics model and its applications to fusion reaction near barrier. *Phys. Rev. C* **65**, 064608 (2002). <https://doi.org/10.1103/PhysRevC.65.064608>
 48. X. Jiang, S. Yan, J.A. Maruhn, Dynamics of energy dissipation in heavy-ion fusion reactions. *Phys. Rev. C* **88**, 044611 (2013). <https://doi.org/10.1103/PhysRevC.88.044611>
 49. K. Zhao, Z. Li, X. Wu et al., Production probability of superheavy fragments at various initial deformations and orientations in the $^{238}\text{U}+^{238}\text{U}$ reaction. *Phys. Rev. C* **88**, 044605 (2013). <https://doi.org/10.1103/PhysRevC.88.044605>
 50. A.V. Karpov, V.V. Saiko, Modeling near-barrier collisions of heavy ions based on a langevin-type approach. *Phys. Rev. C* **96**, 024618 (2017). <https://doi.org/10.1103/PhysRevC.96.024618>

51. V.I. Zagrebaev, A.V. Karpov, W. Greiner, Possibilities for synthesis of new isotopes of superheavy elements in fusion reactions. *Phys. Rev. C* **85**, 014608 (2012). <https://doi.org/10.1103/PhysRevC.85.014608>
52. Z.Q. Feng, G.M. Jin, F. Fu et al., Production cross sections of superheavy nuclei based on dinuclear system model. *Nucl. Phys. A* **771**, 50–67 (2006). <https://doi.org/10.1016/j.nuclphysa.2006.03.002>
53. X.J. Bao, Y. Gao, J.Q. Li et al., Influence of the nuclear dynamical deformation on production cross sections of superheavy nuclei. *Phys. Rev. C* **91**, 011603 (2015). <https://doi.org/10.1103/PhysRevC.91.011603>
54. L. Zhu, W.J. Xie, F.S. Zhang, Production cross sections of superheavy elements $Z=119$ and 120 in hot fusion reactions. *Phys. Rev. C* **89**, 024615 (2014). <https://doi.org/10.1103/PhysRevC.89.024615>
55. G. Adamyan, N. Antonenko, A. Diaz-Torres et al., How to extend the chart of nuclides? *Eur. Phys. J. A* **56**, 1–47 (2020). <https://doi.org/10.1140/epja/s10050-020-00046-7>
56. Z.Q. Feng, H. Ming-Hui et al., Possible way to synthesize superheavy element $Z=117$. *Chin. Phys. Lett.* **24**, 2551 (2007). <https://doi.org/10.1088/0256-307X/24/9/024>
57. Z.Q. Feng, G.M. Jin, J.Q. Li, Influence of entrance channels on the formation of superheavy nuclei in massive fusion reactions. *Nucl. Phys. A* **836**, 82–90 (2010). <https://doi.org/10.1016/j.nuclphysa.2010.01.244>
58. K.X. Cheng, J. Pu, Y.T. Wang et al., Non-frozen process of heavy-ion fusion reactions at deep sub-barrier energies. *Nucl. Sci. Tech.* **33**, 132 (2022). <https://doi.org/10.1007/s41365-022-01114-x>
59. F. Niu, P.H. Chen, Z.Q. Feng, Systematics on production of superheavy nuclei $Z=119$ – 122 in fusion-evaporation reactions. *Nucl. Sci. Tech.* **32**, 103 (2021). <https://doi.org/10.1007/s41365-021-00946-3>
60. M.T. Jin, S.Y. Xu, G.M. Yang et al., Yield of long-lived fission product transmutation using proton-, deuteron-, and alpha particle-induced spallation. *Nucl. Sci. Tech.* **32**, 96 (2021). <https://doi.org/10.1007/s41365-021-00933-8>
61. Y.Q. Xin, N.N. Ma, J.G. Deng et al., Properties of $Z=114$ superheavy nuclei. *Nucl. Sci. Tech.* **32**, 55 (2021). <https://doi.org/10.1007/s41365-021-00899-7>
62. X.B. Yu, L. Zhu, Z.H. Wu et al., Predictions for production of superheavy nuclei with $Z=105$ – 112 in hot fusion reactions. *Nucl. Sci. Tech.* **29**, 154 (2018). <https://doi.org/10.1007/s41365-018-0501-2>
63. Z.Q. Feng, G.M. Jin, J.Q. Li, Production of new superheavy $Z=108$ – 114 nuclei with ^{238}U , ^{244}Pu , and $^{248,250}\text{Cm}$ targets. *Phys. Rev. C* **80**, 057601 (2009). <https://doi.org/10.1103/PhysRevC.80.057601>
64. Z.Q. Feng, G.M. Jin, J.Q. Li et al., Formation of superheavy nuclei in cold fusion reactions. *Phys. Rev. C* **76**, 044606 (2007). <https://doi.org/10.1103/PhysRevC.76.044606>
65. G.G. Adamian, N.V. Antonenko, R.V. Jolos et al., Effective nucleus-nucleus potential for calculation of potential energy of a dinuclear system. *Int. J. Modern Phys. E* **05**, 191–216 (1996). <https://doi.org/10.1142/S0218301396000098>
66. D.L. Hill, J.A. Wheeler, Nuclear constitution and the interpretation of fission phenomena. *Phys. Rev.* **89**, 1102–1145 (1953). <https://doi.org/10.1103/PhysRev.89.1102>
67. V.I. Zagrebaev, Y. Aritomo, M.G. Itkis et al., Synthesis of superheavy nuclei: How accurately can we describe it and calculate the cross sections? *Phys. Rev. C* **65**, 014607 (2001). <https://doi.org/10.1103/PhysRevC.65.014607>
68. W.D. Myers, W.J. Swiatecki, Nuclear masses and deformations. *Nucl. Phys.* **81**, 1–60 (1966). [https://doi.org/10.1016/0029-5822\(66\)90639-0](https://doi.org/10.1016/0029-5822(66)90639-0)
69. C.Y. Wong, Interaction barrier in charged-particle nuclear reactions. *Phys. Rev. Lett.* **31**, 766–769 (1973). <https://doi.org/10.1103/PhysRevLett.31.766>
70. Z.Q. Feng, G.M. Jin, J.Q. Li et al., Production of heavy and superheavy nuclei in massive fusion reactions. *Nucl. Phys. A* **816**, 33–51 (2009). <https://doi.org/10.1016/j.nuclphysa.2008.11.003>
71. J.Q. Li, G. Wolschin, Distribution of the dissipated angular momentum in heavy-ion collisions. *Phys. Rev. C* **27**, 590–601 (1983). <https://doi.org/10.1103/PhysRevC.27.590>
72. J. Li, X. Tang, G. Wolschin, Anticorrelated angular-momentum distributions in heavy-ion collisions. *Phys. Lett. B* **105**, 107–110 (1981). [https://doi.org/10.1016/0370-2693\(81\)91000-5](https://doi.org/10.1016/0370-2693(81)91000-5)
73. G.G. Adamian, N.V. Antonenko, W. Scheid, Characteristics of quasifission products within the dinuclear system model. *Phys. Rev. C* **68**, 034601 (2003). <https://doi.org/10.1103/PhysRevC.68.034601>
74. P. Grangé, L. Jun-Qing, H.A. Weidenmüller, Induced nuclear fission viewed as a diffusion process: Transients. *Phys. Rev. C* **27**, 2063–2077 (1983). <https://doi.org/10.1103/PhysRevC.27.2063>
75. P.H. Chen, Z.Q. Feng, J.Q. Li et al., A statistical approach to describe highly excited heavy and superheavy nuclei. *Chin. Phys. C* **40**, 091002 (2016). <https://doi.org/10.1088/1674-1137/40/9/091002>
76. A.S. Zubov, G.G. Adamian, N.V. Antonenko et al., Competition between evaporation channels in neutron-deficient nuclei. *Phys. Rev. C* **68**, 014616 (2003). <https://doi.org/10.1103/PhysRevC.68.014616>
77. A. Zubov, G.G. Adamian, N. Antonenko et al., Survival probabilities of superheavy nuclei based on recent predictions of nuclear properties. *Eur. Phys. J. A* **23**, 249–256 (2005). <https://doi.org/10.1140/epja/i2004-10089-5>
78. P. Moller, J. Nix, W. Myers et al., Nuclear ground-state masses and deformations. *Atomic Data Nucl. Data Tables* **59**, 185–381 (1995). <https://doi.org/10.1006/adnd.1995.1002>
79. Y.T. Oganessian, V.K. Utyonkov, D. Ibadullayev et al., Investigation of ^{48}Ca -induced reactions with ^{242}Pu and ^{238}U targets at the JINR superheavy element factory. *Phys. Rev. C* **106**, 024612 (2022). <https://doi.org/10.1103/PhysRevC.106.024612>
80. Y.T. Oganessian, V.K. Utyonkov, Y.V. Lobanov et al., Measurements of cross sections and decay properties of the isotopes of elements ^{112}U , ^{114}U , and ^{116}U produced in the fusion reactions $^{233,238}\text{U}$, ^{242}Pu , and $^{248}\text{Cm}+^{48}\text{Ca}$. *Phys. Rev. C* **70**, 064609 (2004). <https://doi.org/10.1103/PhysRevC.70.064609>
81. S. Hofmann, D. Ackermann, S. Antalic et al., The reaction $^{48}\text{Ca} + ^{238}\text{U} \rightarrow ^{286}112^*$ studied at the GSI-SHIP. *Eur. Phys. J. A* **32**, 251–260 (2007). <https://doi.org/10.1140/epja/i2007-10373-x>
82. D. Kaji, K. Morimoto, H. Haba et al., Decay measurement of ^{283}Cn produced in the $^{238}\text{U}(^{48}\text{Ca},3n)$ reaction using GARIS-II. *Journal of the Physical Society of Japan* **86**, 085001 (2017). <https://doi.org/10.7566/JPSJ.86.085001>
83. Y.T. Oganessian, F.S. Abdullin, S.N. Dmitriev et al., Investigation of the $^{243}\text{Am}+^{48}\text{Ca}$ reaction products previously observed in the experiments on elements 113 , 115 , and 117 . *Phys. Rev. C* **87**, 014302 (2013). <https://doi.org/10.1103/PhysRevC.87.014302>
84. Y.T. Oganessian, F.S. Abdullin, S.N. Dmitriev et al., New insights into the $^{243}\text{Am}+^{48}\text{Ca}$ reaction products previously observed in the experiments on elements 113 , 115 , and 117 . *Phys. Rev. Lett.* **108**, 022502 (2012). <https://doi.org/10.1103/PhysRevLett.108.022502>
85. Y.T. Oganessian, V.K. Utyonkov, S.N. Dmitriev et al., Synthesis of elements 115 and 113 in the reaction $^{243}\text{Am}+^{48}\text{Ca}$. *Phys. Rev. C* **72**, 034611 (2005). <https://doi.org/10.1103/PhysRevC.72.034611>

86. L. Stavsetra, K.E. Gregorich, J. Dvorak et al., Independent verification of element 114 production in the $^{48}\text{Ca}+^{242}\text{Pu}$ reaction. *Phys. Rev. Lett.* **103**, 132502 (2009). <https://doi.org/10.1103/PhysRevLett.103.132502>
87. I.I. Gontchar, D.J. Hinde, M. Dasgupta et al., Double folding nucleus-nucleus potential applied to heavy-ion fusion reactions. *Phys. Rev. C* **69**, 024610 (2004). <https://doi.org/10.1103/PhysRevC.69.024610>

Springer Nature or its licensor (e.g. a society or other partner) holds exclusive rights to this article under a publishing agreement with the author(s) or other rightsholder(s); author self-archiving of the accepted manuscript version of this article is solely governed by the terms of such publishing agreement and applicable law.